

## Enhanced functional reversibility in lead-free ferroelectric material over long cycle pyroelectric energy conversion

Chenbo Zhang\*

MOE Key Laboratory of Advanced Micro-Structured Materials, School of Physics Science and Engineering, Institute for Advanced Study, Tongji University, Shanghai 200092, China

Zeyuan Zhu, Ka Hung Chan, Ruhao Huang, and Xian Chen†

Department of Mechanical and Aerospace Engineering, Hong Kong University of Science and Technology, Kowloon, Hong Kong SAR



(Received 22 March 2023; accepted 1 June 2023; published 28 June 2023)

The ferroelectric material usually exhibits temperature-dependent spontaneous polarization, known as pyroelectricity, which can be used to directly convert thermal energy to electricity from ambient low-grade waste heat. When utilizing the structural phase transformations of the material, the conversion capability can be magnified, consequently the device performance can be strongly boosted by orders of magnitude. However, common ferroelectric oxides suffer mechanical fatigue and functional degradation over cyclic phase transformations, hindering widespread applications of the energy conversion device. In this paper, we investigate the mechanical and functional reversibility of the material by lattice tuning and grain coarsening. We discover the lead-free compound  $\text{Ba}(\text{Ce}_{0.005}\text{Zr}_{0.005})\text{Ti}_{0.99}\text{O}_3\text{-}0.10(\text{Ba}_{0.7}\text{Ca}_{0.3})\text{TiO}_3$  ( $\text{BaCeZrTiO}_3\text{-}0.10\text{BaCaTiO}_3$ ) satisfying the compatibility condition among all present phases by its lattice parameters, making the phase transformations highly reversible. We demonstrated that the energy conversion device with equiaxial coarse grains exhibits exceptional fatigue resistance, with stable pyroelectric current output at  $4 \mu\text{A}/\text{cm}^2$  over 3000 energy conversion cycles. Our work opens another way to fabricate high-performance materials that advances the pyroelectric energy conversion for practical applications in engineering.

DOI: [10.1103/PhysRevMaterials.7.064408](https://doi.org/10.1103/PhysRevMaterials.7.064408)

### I. INTRODUCTION

Ferroelectric materials that are easily polarized and show spontaneous polarization are widely used for microelectronic sensors, transducers, and supercapacitors [1–4]. Commonly, the spontaneous polarization of these polar materials is temperature dependent, known as the pyroelectric effect. Utilizing this effect, ferroelectric materials can be used to convert energies directly from heat to electricity, which shows great potential in energy harvesting from low-grade waste heat ( $<150^\circ\text{C}$ ) [5–8]. Recent advances in pyroelectric energy conversion suggest that the phase transformation drives the abrupt change in polarization between the ferroelectric (FE) and paraelectric (PE) phases, thus strongly boosting the electricity generation from the small temperature fluctuations near the transition temperature [6–10]. The frequent thermal exchanges push the core material to transform reversibly between different crystal structures. This conversion is a ferroic, thermal, and mechanical coupled process. Therefore, the loss of transformability and the accumulation of thermal hysteresis over successive energy conversion cycles become the critical issues that prevent it from wide applications and commercialization.

An effective method to enhance phase reversibility is to make the transforming material satisfy the compatibility conditions between phases [11,12]. When the lattice parameters are tuned to satisfy the primary compatibility condition  $\lambda_2 = 1$  where  $\lambda_2$  is the middle eigenvalue of the transformation stretch tensor, the crystal structures of different symmetries can fit together through a stress-free interface during the phase transformation [12–15]. The compatibility condition underlies a material development strategy to suppress functional degradation by lattice parameter tuning, which can be implemented by doping elements with similar physical properties but slightly different ionic radii. The method was initially introduced to develop martensitic alloys [11,16,17], then widely accepted to discover low hysteresis and low functional fatigue transforming ceramics and oxides [18–20]. Several studies have shown that the thermal hysteresis of functional oxides is minimized, simultaneously corresponding to enhanced transport properties when the  $\lambda_2$  value of the material is approaching 1 [7,8,21,22].

Theoretically, achieving kinematic compatibility by lattice design is closely related to the single-crystal behavior under free-boundary conditions. While the material is fabricated into a device integrated with electrodes under the application of thermal, mechanical, and electric coupled loading, the overall performance of the device may depend on the microstructure, crystalline defects, and orientations of the material. In most cases, the device exploits the polycrystalline material, whose grain boundary may influence the multiferroic responses.

\*cbzhang@tongji.edu.cn

†xianchen@ust.hk

Some experimental observations suggest that the coarse grains facilitate the domain switching [23,24]. Over thermally driven transformation cycles, the ferroelectrics with coarse grains usually exhibit a higher phase stability, relatively less electric leakage, and a better pyroelectric property [25–34]. Besides the ferroic properties, it is important to understand and explore how the grain morphology influences the structural, thermal, and mechanical reversibility under stress-induced transformation. During the phase transformation, an internal stress near the phase boundaries will accumulate due to the structural mismatch. When the ferroelectric material is used for energy conversion to harvest the thermal energies stored as temperature fluctuations, the normal stress, mostly in compression, may be developed in the polycrystalline material. To study the mechanical response as well as the phase transformation, reversibility under a stress-induced phase transformation plays an important role in material optimization for the device design. In this paper, we investigate the lead-free ferroelectrics for pyroelectric energy conversion from two perspectives: (1) lattice compatibility and (2) grain morphology. We choose the compound system of barium titanate and barium calcium titanate as the starting point for lattice compatibility tuning. The Ce and Zr doping composition is selected based on our previous study. It was found that equiatomic Ce and Zr enhances the pyroelectric energy conversion output among a series of different compositions [7]. With equiatomic Ce and Zr doping, we aim at searching for an optimal composition of BaCaTiO<sub>3</sub> such that the phase transformations are highly reversible in the system of BaCeZrTiO<sub>3</sub>-*x*BaCaTiO<sub>3</sub>. Once the optimal composition is identified, we will study the effect grain morphologies have on mechanical reversibility and functional reversibility for energy conversion devices. Through these studies, we hope to advance the material development strategy of phase-transforming lead-free ferroelectric materials for energy conversion device fabrication and application.

## II. LEAD-FREE FERROELECTRIC MATERIAL DEVELOPMENT

The phase-transforming ferroelectric system Ba(Ce<sub>0.005</sub>Zr<sub>0.005</sub>)Ti<sub>0.99</sub>O<sub>3</sub>-*x*Ba<sub>0.7</sub>Ca<sub>0.3</sub>TiO<sub>3</sub> (abbreviated as BaCeZrTiO<sub>3</sub>-*x*BaCaTiO<sub>3</sub>) is tuned by varying the atomic ratio *x* ∈ [0.08, 0.12] at. %. The doping elements Ce and Zr were used to suppress the electric leakage [27] and to improve the pyroelectric response [5,21]. The ferroelectric oxides BaCeZrTiO<sub>3</sub> and BaCaTiO<sub>3</sub> are synthesized by a solid-state reaction [7,27], respectively. See the Methods section of Supplemental Material for details [35]. We systematically performed x-ray diffraction for a series of compositions between 0.08BaCaTiO<sub>3</sub> and 0.12BaCaTiO<sub>3</sub> at both cubic and tetragonal phases. Then we refined their lattice parameters and calculated the middle eigenvalue ( $\lambda_2$ ) of the transformation stretch tensor. The value of  $\lambda_2$  given by the composition 0.10BaCaTiO<sub>3</sub> is the closest to 1 among all tested samples, which suggests that the compound BaCeZrTiO<sub>3</sub>-0.10BaCaTiO<sub>3</sub> undergoes the most compatible transformation between ferroelectric and paraelectric phases. Among its nearby compositions between 0.08BaCaTiO<sub>3</sub> and

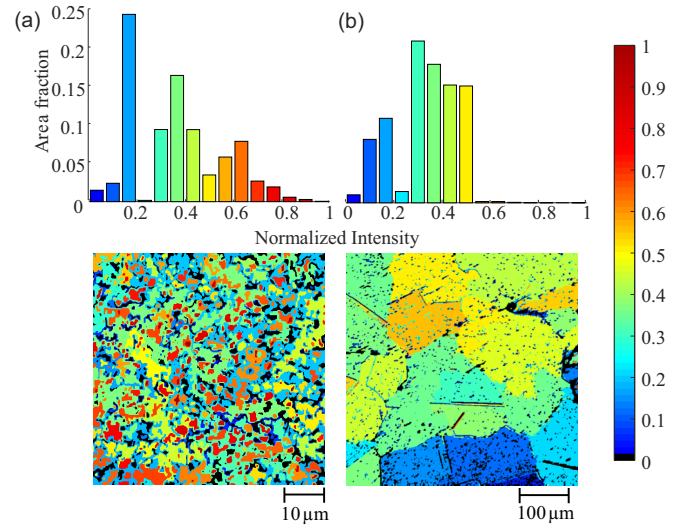


FIG. 1. The histogram of grain morphology and corresponding topographic maps of the BaCeZrTiO<sub>3</sub>-0.10BaCaTiO<sub>3</sub> ferroelectrics sintered by (a) conventional and (b) directional sintering methods, respectively.

0.12BaCaTiO<sub>3</sub>, it shows the lowest thermal hysteresis as seen in Fig. S1 of Supplemental Material [35].

To achieve a different grain morphology, we utilized various sintering methods to sinter the two identical rod-shaped green bodies of BaCeZrTiO<sub>3</sub>-0.10BaCaTiO<sub>3</sub> (see the Methods section of Supplemental Material [35]). One was conventionally sintered using a tube furnace [36], while the other was directionally sintered using a four-mirror infrared image furnace. The green body was sintered through a controlled grain growth by migrating the four-mirror confocal plane slowly. Consequently, a gradual densification was achieved along a uniaxial direction. At a linear migration speed of 3 mm/h, the grains grow much coarser compared to those sintered using the high-temperature tube furnace. After sintering, both rods were transversely cut into thin slices with a thickness of about 1 mm, which were well polished and chemically etched by 37% hydrochloric acid to reveal the grain boundaries. The grain morphology of the sintered rods is studied by a polarized light-reflected differential interference microscope (DInM). For a polar material, the reflectivity depends on the grain orientation, by which we can develop a morphology map of grains. We analyzed the chemical composition and the crystal structure of the specimens by energy-dispersive x-ray spectroscopy (EDS) and x-ray diffraction (XRD) experiments. The lattice parameters of cubic and tetragonal phases as well as the compositions are sufficiently identical between these two specimens sintered by different methods.

## III. RESULTS AND DISCUSSION

### A. Correlation between grain morphology and transport properties

Figure 1 shows the grain morphology of BaCeZrTiO<sub>3</sub>-0.10BaCaTiO<sub>3</sub> observed by DInM, analyzed by the quantitative topographic mapping [37], for specimens with fine grains (FGs) and coarse grains (CGs). The color map of micrographs

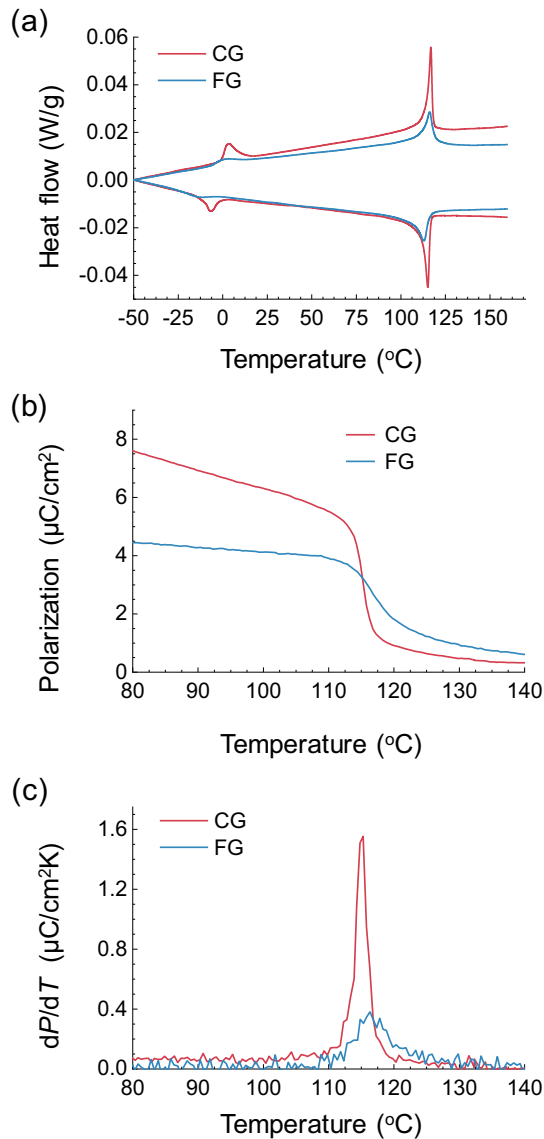


FIG. 2. The comparison of (a) thermal properties, (b) polarization, and (c) pyroelectric coefficient vs temperature between the fine-grained and the coarse-grained BaCeZrTiO<sub>3</sub>-0.10BaCaTiO<sub>3</sub> samples.

indicates grains with varying orientations. We studied the statistics of the areal distribution of the grains, shown as the histograms in Fig. 1. While the specimen with fine grains exhibits a wide range of orientations with a random distribution, the coarse-grained specimen has a preferred orientation for most of its grains. The grain size was presented as the mean diameter of each of the grains sampled from the micrographs. The average grain size is calculated as 1.7 μm for the FG sample and 160 μm for the CG sample. This result confirms the effectiveness of the directional sintering method to achieve the coarse-grained ferroelectric material.

Figure 2 shows that the thermal and transport properties vary drastically as the grain morphology changes. Particularly, the phase transformation features are enhanced in the material with coarse grains. In the CG sample, we can clearly identify two reversible martensitic transformations in Fig. 2(a), that is,

the orthorhombic-to-tetragonal transformation at 0°C and the tetragonal-to-cubic transformation at 115°C. The tetragonal-to-cubic transformation is a first-order phase transformation corresponding to the ferroelectric-to-paraelectric transition as seen in Figs. 2(b) and 2(c). The latent heat of the tetragonal-to-cubic transformation is measured as 0.665 J/g for the coarse-grained sample and 0.514 J/g for the fine-grained sample. The heat exchange due to the phase transformation is about 30% more efficient in the sample with coarse grains, but the transition temperatures are the same for both CG and FG samples. This confirms that the lattice compatibility condition and thermal hysteresis do not depend on the grain morphology. As seen in Fig. 2(a), both samples exhibit 2°C thermal hysteresis for cubic to tetragonal transformation at T<sub>c</sub> = 115°C is usually denoted as the Curie temperature of the ferroelectric material. Near the Curie temperature, the transport properties such as the polarization (P) and pyroelectric coefficient (dP/dT) change abruptly, which also suggests that the material undergoes a first-order phase transformation. The spontaneous polarization in the CG sample is almost twice as that in the FG sample, and the pyroelectric coefficient of the CG sample is 1.55 μC/cm<sup>2</sup>K, enhanced by nearly four times that of the FG sample. According to the performance analysis of the pyroelectric energy conversion device [6,9,28], the CG sample is more suitable for the energy conversion by small temperature differences near the Curie temperature.

## B. Mechanical and functional reversibility of the transforming ferroelectric materials

The mechanical reversibility and durability of the transforming oxides were studied by the micropillar compression experiments for the FG and CG samples, respectively. The cylindrical pillars of 2 μm diameter were fabricated by focused-ion beam (FIB) milling [38], as shown in Fig. 3(a) for fine grains and Fig. 3(b) for coarse grains. Note that the grain size of the CG sample is much larger than the pillar diameter, the micropillar in Fig. 3(b) is a single crystal, while the average grain size of the FG sample is slightly smaller than 2 μm. The FG micropillar may consist of several grains. The microcompression cycles were carried out at 0.5 Hz by force control at room temperature by a Hysitron TI 980 TriboIndenter. In each of the loading/unloading cycles, the pillar was loaded up to 800 μN, then completely unloaded. The experimental details are included in the Methods section of Supplemental Material [35].

As seen in Figs. 3(a) and 3(b) for the stress-strain curves of the micropillars under cyclic loading, the micropillars of both fine grains and coarse grains are mechanically reversible over thousands of loading cycles, providing 0.7% recoverable strains under approximately 300 MPa compressive stress. The mechanical response of the ferroelectric micropillars is nonlinear, which exhibit superelastic behaviors analogous to most of the metallic martensitic materials [39,40], transforming intermetallic compounds [41] and oxides [42–44]. The superelastic strain can be obtained from the nonlinear portion of the stress-strain response as the strain  $\epsilon_T$  in Fig. 3(a) corresponding to the driving stress  $\sigma_T$ . For the FG micropillar,  $\sigma_T = 120$  MPa,  $\epsilon_T = 0.27\%$ . For the CG micropillar, the driving stress  $\sigma_T = 50$  MPa is much lower, associated

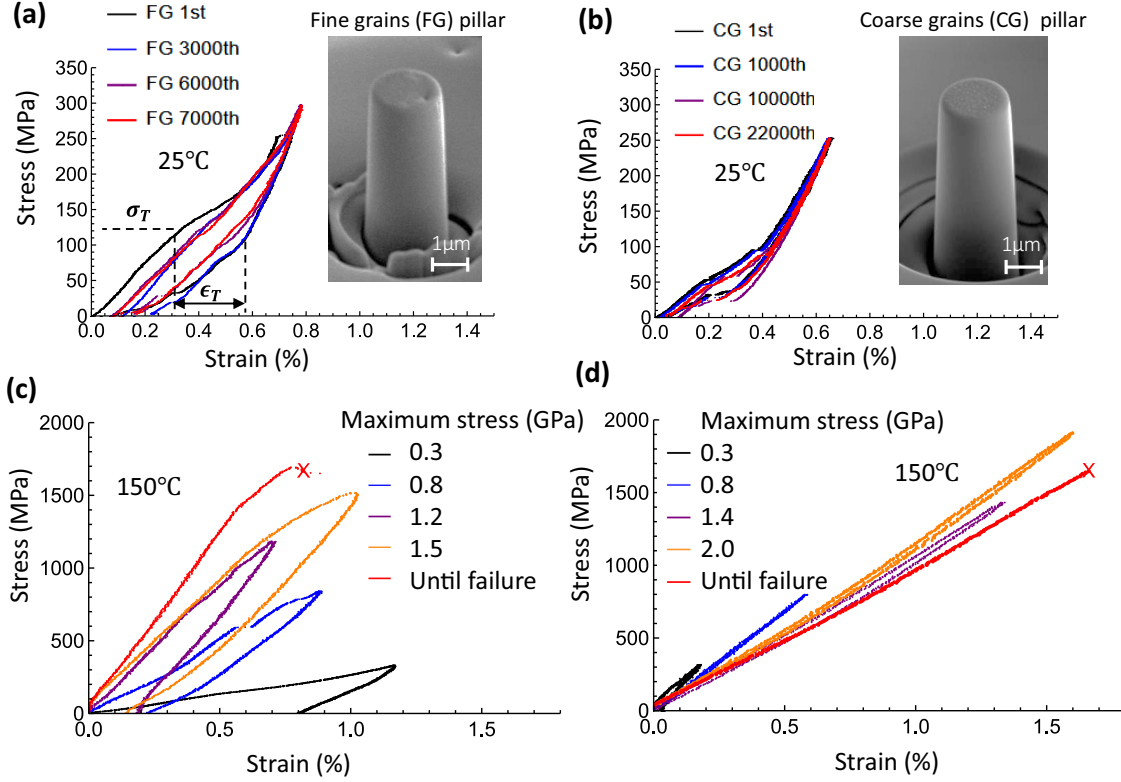


FIG. 3. The stress-strain curves of micropillars fabricated on (a) fine grains (FGs) and (b) coarse grains (CGs) at 25 °C in a ferroelectric phase over uniaxial microcompression cycles. The insets are the scanning electron microscopy (SEM) images of the undeformed micropillars. The stress-strain curves of (c) the FG micropillar and (d) the CG micropillar under uniaxial compression at 150 °C in the paraelectric phase as increasing the maximum compressive stress until structural failure.

with a slightly reduced superelastic strain  $\epsilon_T = 0.2\%$ . For the tetragonal-to-orthorhombic transformation, the transformation stretch tensor can be calculated as  $\sqrt{\mathbf{C}} \in \mathbb{R}^{3 \times 3}$  where  $\mathbf{C}$  denotes the right-hand Cauchy-Green tensor that deforms the tetragonal lattice to the orthorhombic lattice. Depending on the symmetry relation and lattice parameters, there are two possible transformation mechanisms based on the weak Cauchy-Born rule [15], calculated as

$$\mathbf{C} = \begin{cases} \begin{pmatrix} \frac{b_o^2 + c_o^2}{4a_t^2} & 0 & \frac{-b_o^2 + c_o^2}{4a_t c_t} \\ 0 & \frac{a_o^2}{a_t^2} & 0 \\ \frac{-b_o^2 + c_o^2}{4a_t c_t} & 0 & \frac{b_o^2 + c_o^2}{4c_t^2} \end{pmatrix}, & \text{if mechanism I,} \\ \begin{pmatrix} \frac{b_o^2 + c_o^2}{4a_t^2} & \frac{-b_o^2 + c_o^2}{4a_t^2} & 0 \\ \frac{-b_o^2 + c_o^2}{4a_t^2} & \frac{b_o^2 + c_o^2}{4a_t^2} & 0 \\ 0 & 0 & \frac{a_o^2}{c_t^2} \end{pmatrix}, & \text{if mechanism II.} \end{cases} \quad (1)$$

Here,  $a_t = 3.997 \text{ \AA}$  and  $c_t = 4.0314 \text{ \AA}$  are the lattice parameters of the tetragonal phase measured by XRD (see Supplemental Material [35]) and  $a_o = 5.675 \text{ \AA}$ ,  $b_o = 5.69 \text{ \AA}$ , and  $c_o = 3.987 \text{ \AA}$  are the lattice parameters of the orthorhombic phase [45]. For mechanism I, the tetragonal  $a$  axis and the two lateral face diagonals transform to the primitive unit cell of the orthorhombic lattice. The lattice correspondence is

$$[101]_t || [100]_o, \quad [010]_t || [100]_o, \quad [\bar{1}01]_t || [001]_o. \quad (2)$$

For mechanism II, the tetragonal fourfold  $c$  axis and the basal face diagonals transform to the primitive unit cell of the orthorhombic lattice. The lattice correspondence is

$$[110]_t || [001]_o, \quad [1\bar{1}0]_t || [010]_o, \quad [001]_t || [100]_o. \quad (3)$$

The mean transformation strain is calculated as

$$\epsilon_{t0} = \frac{1}{3} \sqrt{(\sqrt{\lambda_1} - 1)^2 + (\sqrt{\lambda_2} - 1)^2 + (\sqrt{\lambda_3} - 1)^2}, \quad (4)$$

where  $\lambda_{1,2,3}$  are the eigenvalues of  $\mathbf{C}$  given in (1). Direct calculation by substituting the lattice parameters gives  $\epsilon_{t0} = 0.00231$  for mechanism I, and  $\epsilon_{t0} = 0.00446$  for mechanism II. Compared to the measured superelastic strain from the FG polycrystalline pillar (i.e.,  $0.27\% = 0.0027$ ), it highly suggests that the superelastic response of the ferroelectric micropillar is attributed to the reversible martensitic transformation by mechanism I in (2).

We calculated the middle eigenvalue of the transformation mechanism I as  $\sqrt{\lambda_2} = 0.9977 \sim 1$ , which satisfies the compatibility condition closely. It suggests that the tetragonal-to-orthorhombic transformation of this material is as compatible as the cubic-to-tetragonal transformation at the Curie temperature. For the single-crystal pillar in the CG sample, it reversibly exhibits the superelasticity over 22 000 compression cycles without any nominal degradation, shown in Fig. 3(b). In contrast, the functional degradation is observed in the polycrystalline pillar with the same level of crystallographic compatibility, shown as the loss of reversibility

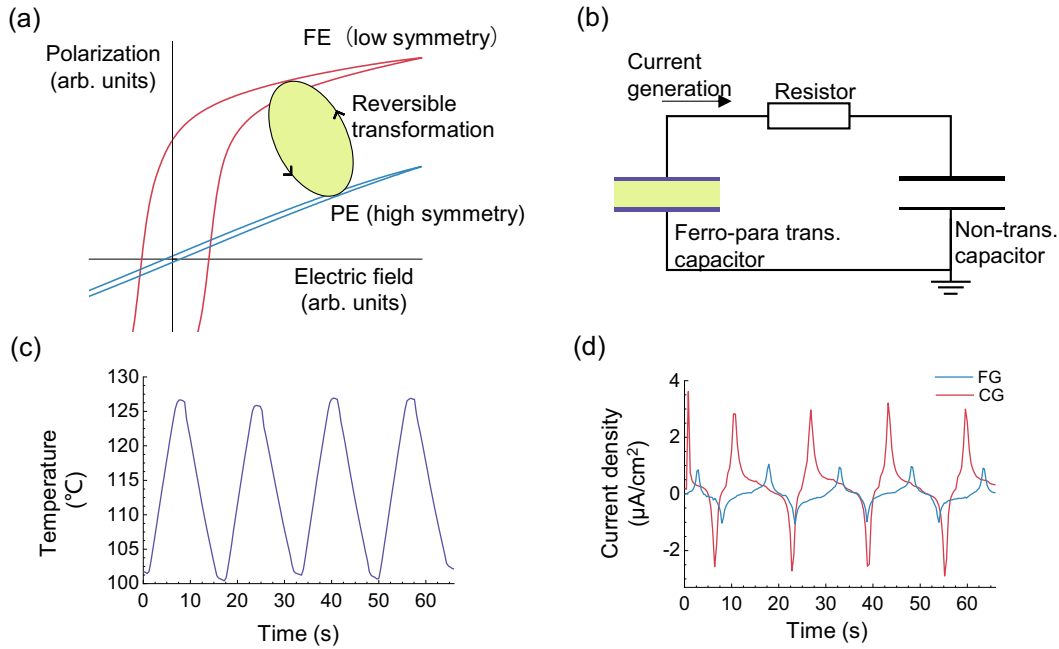


FIG. 4. Demonstration of bias-free pyroelectric energy conversion in  $\text{BaCeZrTiO}_3\text{-}0.10\text{BaCaTiO}_3$  material. (a) Schematics of the bias-free thermodynamic model [5] with (b) the energy pickup circuit to collect generated electricity. (c) Temperature fluctuations between 100 and 125 °C that fully cover the phase transformation between ferroelectric and paraelectric phases. (d) The measured electricity generated by FG and CG samples in the four consecutive conversion cycles.

and the decrease of superelastic strain upon 7000 mechanical cycles, in Fig. 3(a).

Above the Curie temperature, we performed the micromechanical tests to study the overall superelasticity achieved by cubic-to-tetragonal and tetragonal-to-orthorhombic transformations. We adopted the same FIB milling process to fabricate micropillars for both FG and CG samples, respectively. The uniaxial microcompression tests were conducted at 150 °C under the force control by the Triboindenter (Hysitron TI 980). Each of the micropillars was loaded to a preset maximum stress, then completely unloaded. Figures 3(c) and 3(d) show the stress-strain behaviors of the micropillars as the preset maximum stress sequentially increases from 0.3GPa until failure. The mechanical properties of the paraelectric FG and CG pillars are drastically different. The FG micropillar exhibits a large stress hysteresis and irreversible strain upon each of the loading cycles. Finally it fails at 1.6 GPa stress with 0.8% ultimate strain. In contrast, the CG micropillar with the same composition and crystal structure shows an elastic behavior under all loading cycles, finally failing at 1.9 GPa. It is striking that the CG pillar shows 1.6% recoverable strain under nearly 2 GPa compressive stress, which is almost twice the ultimate deformation achieved by the FG pillar. Considering the entire structural transformations from cubic, to tetragonal, and to orthorhombic phases, our experiment discovers that the grain morphology plays a significant role in the mechanical properties and reversibility of the lead-free  $\text{BaCeZrTiO}_3\text{-}0.10\text{BaCaTiO}_3$  system.

### C. Functional reversibility of energy conversion device

The influence of grain morphology on reversibility over the thermally driven energy conversion cycles was studied

by the pyroelectric energy conversion device [7]. The conversion device is particularly designed to harvest the small temperature fluctuations near the Curie temperature of the first-order phase transformation between the cubic paraelectric (PE) and tetragonal ferroelectric (FE) phases. Figure 4(a) elaborates the schematics of a thermodynamic cycle based on the giant pyroelectric effect in the vicinity of the first-order phase transformation [5,6]. This energy conversion system is different from conventional pyroelectric devices [9], as the thermodynamic system does not require an external voltage source to bias the isobaric process at different electric fields for the FE to PE path and the PE to FE path. The energy conversion device was initialized at a polarized state. The detailed device setup is included in the Supplemental Material [35]. The energy pickup circuit is given in Fig. 4(b) [7], with the input thermal energy profile shown in Fig. 4(c) that fluctuates between 100 and 125 °C. The transition temperature of both samples was characterized as 115 °C (Fig. 2), which is fully covered by the temperature fluctuations.

The material performance of our energy conversion is evaluated by the figure of merit [5,7]

$$\text{FOM} = \frac{[P]\kappa}{\ell}, \quad (5)$$

in which  $\kappa = |dP/dT|_{\text{max}}$  is the steepest slope of the polarization with respect to temperature,  $[P]$  is the change of polarization before and after phase transformation, and  $\ell$  is the latent heat of phase transformation. The FOM of  $\text{BaCeZrTiO}_3\text{-}0.10\text{BaCaTiO}_3$  was calculated from the thermal and ferroelectric characterization given by Fig. 2, that is,  $2.44 \mu\text{C}^2/\text{J cm K}$  for the coarse grains and  $0.45 \mu\text{C}^2/\text{J cm K}$  for the fine grains. Consequently, the pyroelectric current density in Fig. 4(d) is measured as  $4.0 \mu\text{A}/\text{cm}^2$  for the coarse

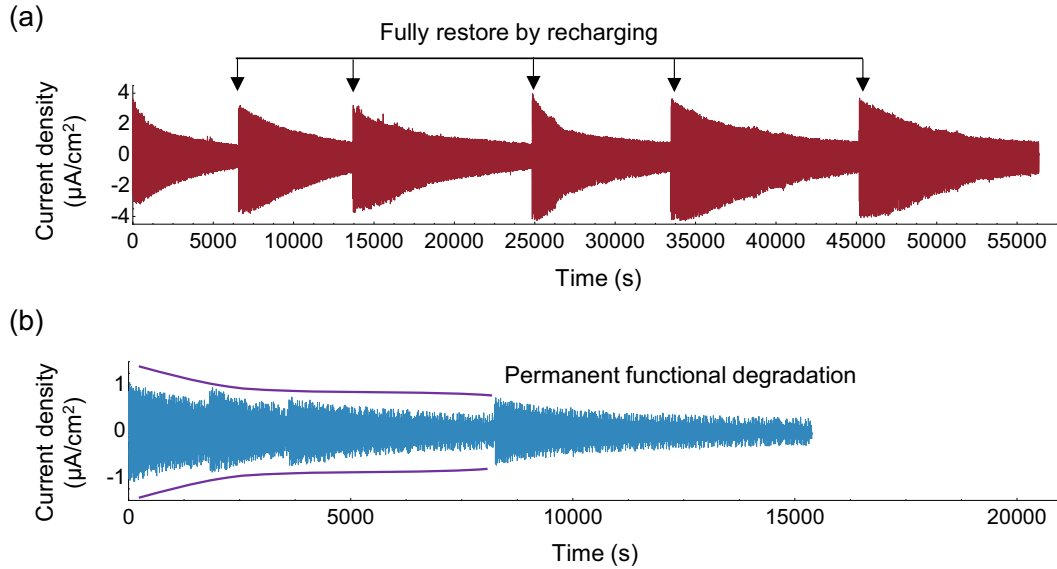


FIG. 5. Characterization of reversibility over thermal cycles by the bias-free pyroelectric energy conversion in  $\text{BaCeZrTiO}_3\text{-}0.10\text{BaCaTiO}_3$  material of different grain sizes. (a) 3392 cycles of energy conversion in coarse-grained (CG) material showing no functional degradation over 55 000 s; (b) functional degradation in the fine-grained (FG) material shows decreased performance.

grains and  $0.8 \mu\text{A}/\text{cm}^2$  for the fine grains, which confirms that the grain coarsening enhances the pyroelectric energy conversion performance for the same material system by a factor of 5, which is consistent with the FOM evaluation in (5). In some literature [46], it was reported that the ferroelectric behavior can be much improved at the morphotropic phase boundary (MPB). However, the  $\text{BaCaTiO}_3$  composition of our material system is far away from the MPB. We conjecture that the grain morphology and crystallographic compatibility are the primary factors to enhance the pyroelectric energy conversion performance in our device. The functional reversibility over long energy conversion cycles is characterized in Fig. 5. As the developed ferroelectric compound satisfies the lattice compatibility for both ferroelectric and paraelectric phases, both FG and CG pyroelectric devices exhibit good functional reversibility upon thousands of conversion cycles. Specifically, the coarse-grained sample with better mechanical reversibility and lower hysteresis stably and continuously generates approximately  $4 \mu\text{A}/\text{cm}^2$  pyroelectric current density over 3000 conversion cycles lasting about 15 h, in Fig. 5(a). As seen, the converted electric energy decays over time due to the unavoidable electric leakage of the dielectric material [27], but this is not the intrinsic fatigue of the functional material. During conversion, we just need to reset the device periodically by recharging the transforming pyroelectric capacitor to its initial state, called an e-pack period [7]. As a result, the energy generation capacity is completely reversed to the reference value if the phase-transforming material sustains its functionality. Upon five e-pack periods, Fig. 5(a) shows that the coarse-grained pyroelectric device still generates the pyroelectric current at the same level as in its first few cycles. However, the fine-grained pyroelectric device shows a clear trend of functional degradation besides the electric leakage in Fig. 5(b). That is the reference pyroelectric current becomes smaller and smaller in each of the e-pack periods. Finally, the functionality

degrades to half of the pyroelectric current produced in the first cycle after 15 000 s (i.e., 4 h), which implies that the phase-transforming ferroelectric layer of the pyroelectric device has irreversibly lost its energy conversion capability. Table I summarizes the mechanical and functional properties of both FG and CG pyroelectric energy conversion devices, suggesting that the crystallographic compatible CG material with approximately equiaxial  $160\text{-}\mu\text{m}$ -sized grains is an ideal material candidate for pyroelectric energy conversion by phase transformation.

#### IV. CONCLUSION

Energy harvesting from heat energies in the low-temperature regime (i.e.,  $<200^\circ\text{C}$ ) is an interdisciplinary and multifaceted grand challenge in energy science. The rational design of functional materials is undoubtedly one of the key imperatives. In this paper, we introduced and demonstrated an effective development strategy to enhance the material properties for energy conversion at two levels: (1) to make the lattice parameters of phases satisfy the kinematic compatibility condition by compositional tuning

TABLE I. Comparison of the microstructure, mechanical, and energy conversion properties of the  $\text{BaCeZrTiO}_3\text{-}0.10\text{BaCaTiO}_3$  ferroelectric material.

Properties	$\text{BaCeZrTiO}_3\text{-}0.10\text{BaCaTiO}_3$	
	FG	CG
Grain size ( $\mu\text{m}$ )	1.67	160
$\sigma_{\text{max}}$ (GPa)	1.70	1.91
$dP/dT$ at $T_c$ ( $\mu\text{C}/\text{cm}^2 \text{K}$ )	0.38	1.55
FOM ( $\mu\text{C}^2/\text{J cm K}$ )	0.45	2.44
$i_p$ ( $\mu\text{A}/\text{cm}^2$ )	0.8	4.0

and (2) to coarsen the grains (i.e., over 150  $\mu\text{m}$ ) effectively by a directional sintering method. We proposed the lead-free  $\text{BaCeZrTiO}_3\text{-}0.10\text{BaCaTiO}_3$  exhibits exceptionally good mechanical reversibility and high mechanical strength by satisfying the compatibility condition closely for the entire transformation regime. The pyroelectric device comprised of equiaxial coarse grains significantly enhances the energy conversion performance by nearly five times, compared to the fine-grained device. In addition, the coarse-grained device are running over tens of thousands of transformation cycles with stable and continuous pyroelectric current output at the microampere level. Our work opens a way to effectively discover high-performance pyroelectric material with strong mechanical reversibility, which significantly advances the application

and commercialization of the pyroelectric energy conversion by small temperature fluctuations.

#### ACKNOWLEDGMENTS

C.Z. acknowledge the support by National Natural Science Foundation of China (No. 12204350), Fundamental Research Funds for the Central Universities (No. 22120220252, No. 22120230041). X.C., Z.Z., K.H.C., and R.H. are thankful for the financial support under GRF Grants No. 16203021 and No. 16204022 and CRF Grant No. C6016-20G-C by Research Grants Council, Hong Kong. X.C. and C.Z. are thankful for the support by Innovation and Technology Commission, HK through the ITF Seed Grant No. ITS/354/21.

- 
- [1] S.-H. Shin, D. H. Park, J.-Y. Jung, M. H. Lee, and J. Nah, Ferroelectric zinc oxide nanowire embedded flexible sensor for motion and temperature sensing, *ACS Appl. Mater. Interfaces* **9**, 9233 (2017).
- [2] W. Gao, Y. Zhu, Y. Wang, G. Yuan, and J.-M. Liu, A review of flexible perovskite oxide ferroelectric films and their application, *J. Materiomics* **6**, 1 (2020).
- [3] I. Kanno, Piezoelectric MEMS: Ferroelectric thin films for MEMS applications, *Jpn. J. Appl. Phys.* **57**, 040101 (2018).
- [4] K. T. Butler, J. M. Frost, and A. Walsh, Ferroelectric materials for solar energy conversion: photoferroics revisited, *Energy Environ. Sci.* **8**, 838 (2015).
- [5] C. Zhang, Y. Song, M. Wegner, E. Quandt, and X. Chen, Power-Source-Free Analysis of Pyroelectric Energy Conversion, *Phys. Rev. Appl.* **12**, 014063 (2019).
- [6] A. Bucsek, W. Nunn, B. Jalan, and R. D. James, Direct Conversion of Heat to Electricity Using First-Order Phase Transformations in Ferroelectrics, *Phys. Rev. Appl.* **12**, 034043 (2019).
- [7] C. Zhang, Z. Zeng, Z. Zhu, N. Tamura, and X. Chen, Energy Conversion from Heat to Electricity by Highly Reversible Phase-Transforming Ferroelectrics, *Phys. Rev. Appl.* **16**, 024064 (2021).
- [8] C. Zhang, Z. Zhu, J. Y. Choi, J. Y. Kim, and X. Chen, Low hysteresis and enhanced figure-of-merit of pyroelectric energy conversion at compatible phase transformation, *Appl. Phys. Lett.* **119**, 082902 (2021).
- [9] C. R. Bowen, J. Taylor, E. LeBoulbar, D. Zabeck, A. Chauhan, and R. Vaish, Pyroelectric materials and devices for energy harvesting applications, *Energy Environ. Sci.* **7**, 3836 (2014).
- [10] A. N. Bucsek, W. Nunn, B. Jalan, and R. D. James, Energy conversion by phase transformation in the small-temperature-difference regime, *Annu. Rev. Mater. Res.* **50**, 283 (2020).
- [11] Y. Song, X. Chen, V. Dabade, T. W. Shield, and R. D. James, Enhanced reversibility and unusual microstructure of a phase-transforming material, *Nature (London)* **502**, 85 (2013).
- [12] X. Chen, V. Srivastava, V. Dabade, and R. D. James, Study of the cofactor conditions: Conditions of supercompatibility between phases, *J. Mech. Phys. Solids* **61**, 2566 (2013).
- [13] Z. Zhang, R. D. James, and S. Müller, Energy barriers and hysteresis in martensitic phase transformations, *Acta Mater.* **57**, 4332 (2009).
- [14] J. M. Ball and R. D. James, Fine phase mixtures as minimizers of energy, in *Analysis and Continuum Mechanics* (Springer, Berlin, 1989), pp. 647–686.
- [15] K. Bhattacharya, *Microstructure of Martensite: Why it Forms and How it Gives Rise to the Shape-Memory Effect*, Vol. 2 (Oxford University Press, Oxford, UK, 2003).
- [16] J. Cui, Y. S. Chu, O. O. Famodu, Y. Furuya, J. Hattrick-Simpers, R. D. James, A. Ludwig, S. Thienhaus, M. Wuttig, Z. Zhang, and I. Takeuchi, Combinatorial search of thermoelastic shape-memory alloys with extremely small hysteresis width, *Nat. Mater.* **5**, 286 (2006).
- [17] H. Gu, L. Bumke, C. Chluba, E. Quandt, and R. D. James, Phase engineering and supercompatibility of shape memory alloys, *Mater. Today* **21**, 265 (2018).
- [18] E. L. Pang, C. A. McCandler, and C. A. Schuh, Reduced cracking in polycrystalline  $\text{ZrO}_2\text{-CeO}_2$  shape-memory ceramics by meeting the cofactor conditions, *Acta Mater.* **177**, 230 (2019).
- [19] J. Jetter, H. Gu, H. Zhang, M. Wuttig, X. Chen, J. R. Greer, R. D. James, and E. Quandt, Tuning crystallographic compatibility to enhance shape memory in ceramics, *Phys. Rev. Mater.* **3**, 093603 (2019).
- [20] H. Gu, J. Rohmer, J. Jetter, A. Lotnyk, L. Kienle, E. Quandt, and R. D. James, Exploding and weeping ceramics, *Nature (London)* **599**, 416 (2021).
- [21] M. Wegner, H. Gu, R. D. James, and E. Quandt, Correlation between phase compatibility and efficient energy conversion in Zr-doped barium titanate, *Sci. Rep.* **10**, 3496 (2020).
- [22] Y. G. Liang, S. Lee, H. S. Yu, H. R. Zhang, Y. J. Liang, P. Y. Zavalij, X. Chen, R. D. James, L. A. Bendersky, A. V. Davydov, X. H. Zhang, and I. Takeuchi, Tuning the hysteresis of a metal-insulator transition via lattice compatibility, *Nat. Commun.* **11**, 3539 (2020).
- [23] W. Cao and C. A. Randall, Grain size and domain size relations in bulk ceramic ferroelectric materials, *J. Phys. Chem. Solids* **57**, 1499 (1996).
- [24] X. Li and J. Wang, Effect of grain size on the domain structures and electromechanical responses of ferroelectric polycrystal, *Smart Mater. Struct.* **26**, 015013 (2017).
- [25] W. Zhang and K. Bhattacharya, A computational model of ferroelectric domains. Part II: Grain boundaries and defect pinning, *Acta Mater.* **53**, 199 (2005).

- [26] G. Liu, S. Zhang, W. Jiang, and W. Cao, Losses in ferroelectric materials, *Mat. Sci. Eng., R* **89**, 1 (2015).
- [27] C. Zhang, Z. Zeng, Z. Zhu, M. Karami, and X. Chen, Impact of Leakage for Electricity Generation by Pyroelectric Converter, *Phys. Rev. Appl.* **14**, 064079 (2020).
- [28] Q. Zhang, W. Cai, Q. Li, R. Gao, G. Chen, X. Deng, Z. Wang, X. Cao, and C. Fu, Enhanced piezoelectric response of (Ba,Ca)(Ti,Zr)O<sub>3</sub> ceramics by super large grain size and construction of phase boundary, *J. Alloys Compd.* **794**, 542 (2019).
- [29] L. Yingwei, C. Xiangyang, Z. Dapeng, and G. Zhipeng, Influence of domain switching process on the electrical fatigue behavior of ferroelectrics, *Ceram. Int.* **46**, 24213 (2020).
- [30] C. Mao, S. Yan, S. Cao, C. Yao, F. Cao, G. Wang, X. Dong, X. Hu, and C. Yang, Effect of grain size on phase transition, dielectric and pyroelectric properties of BST ceramics, *J. Eur. Ceram. Soc.* **34**, 2933 (2014).
- [31] Y. Chen, H. Ye, X. Wang, Y. Li, and X. Yao, Grain size effects on the electric and mechanical properties of submicro BaTiO<sub>3</sub> ceramics, *J. Eur. Ceram. Soc.* **40**, 391 (2020).
- [32] X. Moya, E. Stern-Taulats, S. Crossley, D. González-Alonso, S. Kar-Narayan, A. Planes, L. Mañosa, and N. D. Mathur, Giant electrocaloric strength in single-crystal BaTiO<sub>3</sub>, *Adv. Mater.* **25**, 1360 (2013).
- [33] Y. Huan, X. Wang, J. Fang, and L. Li, Grain size effect on piezoelectric and ferroelectric properties of BaTiO<sub>3</sub> ceramics, *J. Eur. Ceram. Soc.* **34**, 1445 (2014).
- [34] Z. Hanani, D. Mezzane, M. Amjoud, S. Fourcade, A. G. Razumnaya, I. A. Luk'Yanchuk, and M. Gouné, Enhancement of dielectric properties of lead-free BCZT ferroelectric ceramics by grain size engineering, *Superlattices Microstruct.* **127**, 109 (2019).
- [35] See Supplemental Material at <http://link.aps.org/supplemental/10.1103/PhysRevMaterials.7.064408> for methods and materials for synthesis, thermal and mechanics characterization, x-ray diffraction characterization, and energy conversion device setup, which includes Refs. [5,7].
- [36] A. Dupuy, Y. Kodera, G. Carman, and J. Garay, Effect of phase homogeneity and grain size on ferroelectric properties of 0.5Ba(Zr<sub>0.2</sub>Ti<sub>0.8</sub>)O<sub>3</sub>-0.5(Ba<sub>0.7</sub>Ca<sub>0.3</sub>)TiO<sub>3</sub> (BXT) lead-free ceramics, *Scr. Mater.* **159**, 13 (2019).
- [37] Z. Zeng, H.-C. Chiu, L. Zhao, T. Zhao, C. Zhang, M. Karami, H. Yu, S. Du, and X. Chen, Dual beam-shear differential interference microscopy for full-field surface deformation gradient characterization, *J. Mech. Phys. Solids* **145**, 104162 (2020).
- [38] M. Karami, Z. Zhu, Z. Zeng, N. Tamura, Y. Yang, and X. Chen, Two-tier compatibility of superelastic bicrystal micropillar at grain boundary, *Nano Lett.* **20**, 8332 (2020).
- [39] R. Manjeri, S. Qiu, N. Mara, A. Misra, and R. Vaidyanathan, Superelastic response of [111] and [101] oriented NiTi micropillars, *J. Appl. Phys.* **108**, 023501 (2010).
- [40] M. Karami and X. Chen, Nanomechanics of shape memory alloys, *Mat. Today Adv.* **10**, 100141 (2021).
- [41] J. T. Sypek, H. Yu, K. J. Dusoe, G. Drachuck, H. Patel, A. M. Giroux, A. I. Goldman, A. Kreyssig, P. C. Canfield, S. L. Bud'ko, C. R. Weinberger, and S.-W. Lee, Superelasticity and cryogenic linear shape memory effects of CaFe<sub>2</sub>As<sub>2</sub>, *Nat. Commun.* **8**, 1083 (2017).
- [42] A. Lai, Z. Du, C. L. Gan, and C. A. Schuh, Shape memory and superelastic ceramics at small scales, *Science* **341**, 1505 (2013).
- [43] Y. Li, K. Chu, C. Liu, P. Jiang, K. Qu, P. Gao, J. Wang, F. Ren, Q. Sun, L. Chen, and J. Li, Superelastic oxide micropillars enabled by surface tension-modulated 90° domain switching with excellent fatigue resistance, *Proc. Natl. Acad. Sci. USA* **118**, e2025255118 (2021).
- [44] E. Camposilvan and M. Anglada, Size and plasticity effects in zirconia micropillars compression, *Acta Mater.* **103**, 882 (2016).
- [45] R. Rhodes, Barium titanate twinning at low temperatures, *Acta Crystallogr.* **4**, 105 (1951).
- [46] W. Liu and X. Ren, Large Piezoelectric Effect in Pb-Free Ceramics, *Phys. Rev. Lett.* **103**, 257602 (2009).